Extreme Mechanics Letters 29 (2019) 100463

Contents lists available at ScienceDirect

Extreme Mechanics Letters

journal homepage: www.elsevier.com/locate/eml

Selectively aligned cellulose nanofibers towards high-performance soft actuators

Yudi Kuang [a,b,1], Chaoji Chen [b,1], Jian Cheng [c,1], Glenn Pastel [b], Tian Li [b], Jianwei Song [b], Feng Jiang [b], Yiju Li [b], Ying Zhang [b], Soo-Hwan Jang [b], Gang Chen [a], Teng Li [c,*], Liangbing Hu [b,*]

[a] State Key Laboratory of Pulp and Paper Engineering, South China University of Technology, Guangzhou, 510640, China
[b] Department of Materials Science and Engineering, University of Maryland, College Park, MD, 20742, United States
[c] Department of Mechanical Engineering, University of Maryland, College Park, MD, 20742, United States

ARTICLE INFO

Article history:
Received 19 December 2018
Received in revised form 20 March 2019
Accepted 10 April 2019
Available online 4 May 2019

Keywords:
Soft actuator
Coffee ring effect
Functionally patterned microstructure
Cellulose nanofiber
Biopolymer

ABSTRACT

Motion of plants in response to environment stimuli (e.g., opening and closing of pinecones) often finds its origin in the organized microscopic structures of the moving part, which sheds light on a new way to design and fabricate high-performance biomimetic soft actuators. In this paper, we design a micro-patterned soft actuator consisting of a selectively aligned cellulose nanofiber layer and a passivation layer. The unique structure of the cellulose nanofiber layer is achieved by an evaporation-assisted self-assembly method (inspired by the "coffee ring" effect). Benefiting from the hydrophilic, nanoporous and well-aligned cellulose nanofiber network, the resultant soft actuator demonstrates a fast (response time less than 1s), extremely powerful (~1000 times lifting weight ratio), and controllable response to external environmental stimuli, which is comparable to the best performing soft actuators reported in the literature. Mechanics modeling further reveals that the well-aligned cellulose nanofiber layer plays an important role in both the final curvature and generation of the actuation forces. Proof-of-concept demonstrations of the micro-patterned soft actuators as mechanical arms and soft walking robots indicate their great potential for soft robots and biomimetic systems.

1. Introduction

Soft actuators responsive to external stimuli are of great interest for both fundamental research and potential applications such as artificial muscular systems [1–3], soft robots [4,5], and energy generators [6–8]. During the past decades, soft actuators with diverse structures and multi-functional stimuli-responsive properties have been demonstrated, including pneumatic actuators [9,10], electric-responsive actuators [11–17] thermal-responsive actuators [18–20], light-responsive actuators [21–23], magnetic-responsive actuators [24], and solvent/chemical-responsive actuators [25–27], etc. In particular, bilayer actuators that utilize the asymmetric deformation coefficients of the active and passive layers in response to external stimuli have emerged as promising candidates in the fabrication of soft actuators, owing to their simple production process and universal adaptivity [28–34]. However, in traditional bilayer soft actuators the homogeneous polymer with isotropic volume change in the active layer always results in imprecise movements and small displacements under a weakly generated driving force.

In nature, there exist inspiring examples of environment-driven plant movements with well-controlled moving direction and powerful force generation, such as the opening-closing of pinecones and the twisting–untwisting of Bauhinia variegata pods [35–37]. Plant anatomy found that the advanced plant movements are coming from their microtissues with functionally patterned microstructure. Inspired by this, tremendous strides have been made to imitate the specially arranged microstructure of natural plant systems to improve the response properties of traditional soft actuator. For example, liquid crystal polymer actuators with aligned, polymerized mesogenic molecules demonstrated anisotropic contraction and expansion, mostly perpendicular to the alignment direction [38]. By embedding aligned reinforcing fibers, such as carbon nanotubes or glass fibers, in an active matrix or a single layer of the asymmetric bilayer actuator, diverse deformations have also been achieved [39,40]. Other fabrication methods, such as electrospinning and surface modification [41–43], have also been demonstrated to fabricate soft actuators with patterned microstructures and enhanced response properties. Nevertheless, despite the achievements in functional

* Corresponding authors.
E-mail addresses: lit@umd.edu (T. Li), binghu@umd.edu (L. Hu).
[1] These authors contributed equally to this work.

https://doi.org/10.1016/j.eml.2019.100463
2352-4316/

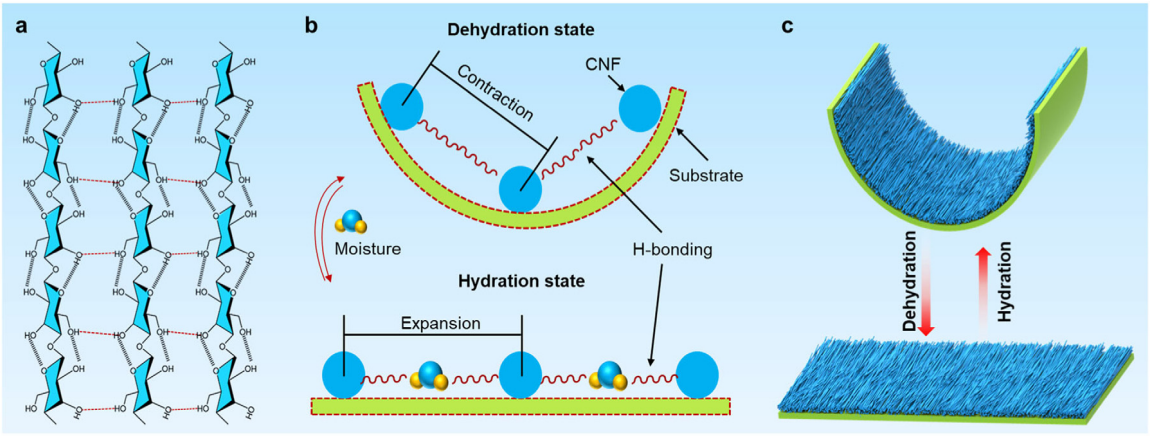

Fig. 1. Illustration of the soft bilayer CNF-soft actuator with a selectively aligned CNF layer prepared by evaporation-assisted self-assembly. (a) Schematic illustrating the intra-/inter-molecular H-bonding between the cellulose molecular chains. (b) Simplified schematics illustrating the hydration/dehydration induced micro-level space change between three parallel CNFs. (c) Schematics illustrating the hydration/dehydration induced macro-level actuation behavior of the CNF-actuator.

microstructure design, these soft actuators still suffer from shortcomings such as costly raw materials, strict or complex synthesis technology and equipment, and inadequate responsiveness. As a result, a low-cost, universal, and easy to scale-up strategy for high-performance soft actuators remain arduous.

Here, we design a micro-patterned soft actuator based on a passive substrate covered with selectively aligned cellulose nanofibers (CNFs). The unique structure of the CNF layer is achieved by a straightforward solvent evaporation-assisted self-assembly method. Ascribed to the micro-patterned structure and disparate hygroscopicity of the CNFs and passivation layers, the resultant CNF-actuator demonstrates well-controlled, rapid (response time less than 1 s), and extremely powerful (∼1000 times lifting weight ratio) actuation in response to temperature and humidity of the external environment. Given the widely available raw materials, scalable productivity, as well as the excellent response properties, our micro-patterned CNF-actuator can become a promising candidate for use in soft robots and other biomimetic systems.

2. Results and discussion

2.1. Construction of selectively aligned CNF-soft actuator

CNFs are prepared by disintegrating low-cost, renewable, and abundant wood fibers via a mature chemomechanical treatment process widely used in the paper-making industry (Fig. S1–S4). Compared with micro-sized cellulose fiber, nano-sized CNFs possess more exposed hydrophilic hydroxyl groups (-OH) due to a larger specific surface area. The increased surface hydroxyl groups promise more inter-molecular hydrogen bonding (H-bonding) between the individual CNFs (Fig. 1a), enabling the formation of CNF percolation network with superior mechanical strength (up to hundreds of MPa stress and tens of GPa modulus) in drying state. Meanwhile, H-bonding as a kind of super-molecular bond can be reversibly broken and re-formed under the attack of water molecular, causing the space change between the CNFs and the mechanical adaptive of the CNF film (Fig. 1b). Based on this mechanism, we are able to prepare uniaxially responsive CNFs film by controlling the force direction of the H-bonding via the alignment of the CNFs. To assemble the randomly dispersed one-dimensional fibrils, our work exploits a simple but efficient solvent evaporation-assisted self-assembly method derived from the "coffee ring" effect. Selectively aligned CNF-soft actuator can be simply prepared by rationally depositing CNF suspension on a polyimide (PI) substrate followed by a static drying process (Fig. S5). The solvent evaporation induces capillary flow during the drying process then drives the assembly of high aspect ratio CNF into an anisotropic structure oriented perpendicular to the perimeter of the deposition from the edge to the center, as shown in Fig. 1c. Upon temperature or humidity stimuli, such a readily arranged nanostructure can enhance the contraction/expansion of CNF layer perpendicular to the axial direction of CNFs, leading to a rapid and powerful bidirectional bending of the CNF-soft actuator.

2.2. Anisotropic assembly of CNFs

The formation mechanism of the anisotropic CNF layer is attributed to the evaporation-assisted circulation and unique rheological properties of the CNF suspension. More explicitly, the deposition of CNF on the PI substrate can be divided into three steps, as shown in Fig. 2a: (i) thickening and orienting of the CNF colloidal system; (ii) gelation and deposition; and (iii) fast drying into a selectively aligned film. In the first step, the low concentration CNF suspension with a low viscosity slowly thickens and pins the solid–liquid–gas interfaces to an initial position. The gradient in evaporation flux from the edge (high) to the center (low) caused by the wedge geometry leads to a circulating flow and forces the CNF to move with the capillary flow [44]. The concomitant movement aligns the CNF but is different from the ring-like solute deposition of other colloid systems. The CNF suspension deposits with uniform thickness due to the concentration-induced gelation process (Fig. S6–S7). Shrinkage after evaporation of the solvent not only increases the steric hindrance but also shortens the distance between the individual CNF and leads to more physical entanglement and intermolecular hydrogen bonding. Finally, a physically crosslinked CNF gel network is formed with restricted mobility which inhibits the formation of rings during the deposition (Fig. S8a–d). The gelation process also helps preserve the preformed fiber orientation until the final drying process.

To further confirm the capillary flow of the CNF suspension during the air-drying process, 5 wt% hydrophobic carbon nanotubes (CNTs) are pre-mixed into the suspension as a visible tracer and the substrate is also replaced by a transparent polyethylene terephthalate (PET) film for better contrast. CNTs are more likely to flow in the direction of the capillary forces due to the weak conflicting interactions between CNT–CNT and CNT–CNF imparted by the hydrophobicity of CNT. A visible ring stain is observed along the perimeter of the CNF deposition while drying, which suggests the existence of capillary flow (Fig. 2b and Fig. S9). Scanning electron microscopy (SEM) images clearly show

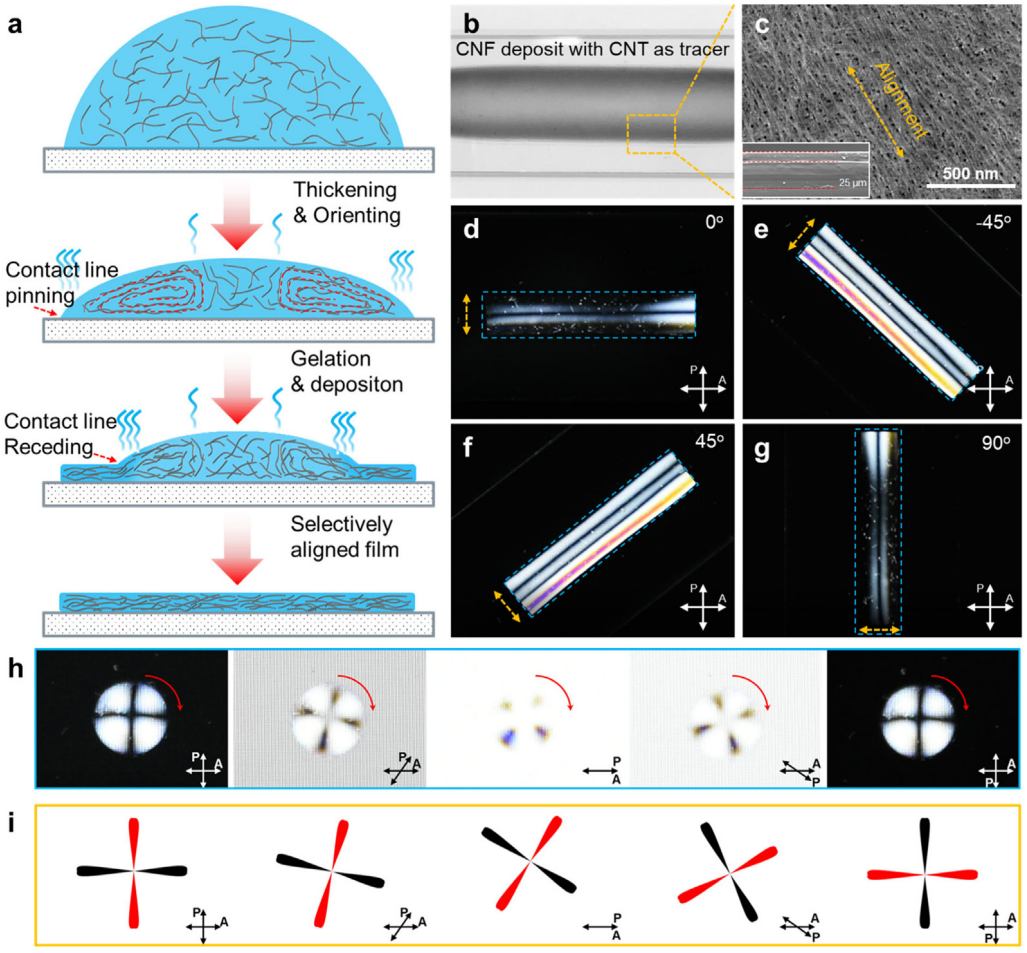

Fig. 2. Solvent evaporation-assisted self-assembly of CNFs and characterization of the resultant CNF-soft actuator. (a) Schematics showing the formation of the selectively aligned CNF film on a substrate. (b) Photographs of the CNF deposition with a few CNTs as a visible tracer on top of a transparent PET film. (c) Top-view SEM images showing the anisotropic CNFs arrangement of the CNF-soft actuator, respectively. Inset shows the cross-section of the obtained bilayer CNF-soft actuator with a thin layer of cellulose on top of the substrate. (d–g) Polarized optical images of the anisotropic CNF deposition. By rotating the CNF deposition sample, variations between the bright and dark field of view are observed every 90°, indicating the CNFs are well aligned. (h) Polarizing optical images and corresponding (i) schematics illustrating the schlieren texture of the circular CNF deposition under crossed polarized light. The arrow represents the rotation direction of the polarizer.

the aligned distribution of CNFs in the deposition (Fig. 2c and Figs. S8 and S10). Besides the anisotropic arrangement, it is worth noting that the CNF layer is observed to be full of nanopores, which paves the way for rapid adsorption/desorption of water molecules (Fig. S11).

Polarizing optical images (POM) further confirm the anisotropic arrangement of CNFs in the deposition. The large brightness difference observed between Fig. 2d–e indicates the anisotropic alignment of CNFs in the deposition layer. The light becomes linearly polarized after passing through the first polarizer. When the second polarizer is placed in a crossed direction, the light shall not be transmitted. Thus the background field appears dark. When the CNF arrangement direction aligns perfectly with either of the polarizers, the optical transmittance should still be negligible, as indicated in Fig. 2d and 2g (the small bright area in the center and the end area is because of the natural instability of the solvent evaporation process). When the CNF alignment direction is 45° titled, the transmitted light becomes partially polarized in both direction but can still be transmitted. By rotating the CNF deposition sample, the dark regions at 0° and 90° turn to be bright white with the colored band after 45° rotation (Fig. 2e–f, Movie S1), indicating a well organized unidirectional alignment of CNFs in the deposition.

A schlieren texture is also observed when the CNF deposition is designed to be a circle. By rotating one of the polarizers, the schlieren brushes appear to rotate the same direction as the polarizer (Fig. 2h–i, Movie S2), suggesting that the CNFs is aligned perpendicular to the periphery of the deposition. To better understand the geometric limit on the assembly behavior of the CNF droplet, we further performed *in-situ* POM characterization of the CNF droplets with different diameters, as shown in Fig. S12. The results found that the CNFs demonstrate a better alignment (a perfect cross, schlieren texture) when the diameter of the CNF droplet is smaller than 5 mm, while with the increase of the droplet diameter, a twisted and dark cross is observer at the center of the deposition (Fig. S12a–b). This observation is consistent with our previous discussion, that is, the solvent-induced self-assembly of the CNF droplet is geometrically limited, where the capillary flow mainly occurs in the curved projection area of the droplet, as shown in Fig. S12c–d. When the size of the droplet increases, the center area becomes flat so that no capillary follow happens there, resulting in a random CNFs deposition area in the center.

2.3. Stimuli-responsive behaviors of CNF-soft actuator

Fig. 3a illustrates typical bending displacements of the CNF-soft actuator with one end fixed upon exposure to a high temperature and low humidity environment. Volume contraction caused by dehydration of the CNF layer drives the strip-like actuator

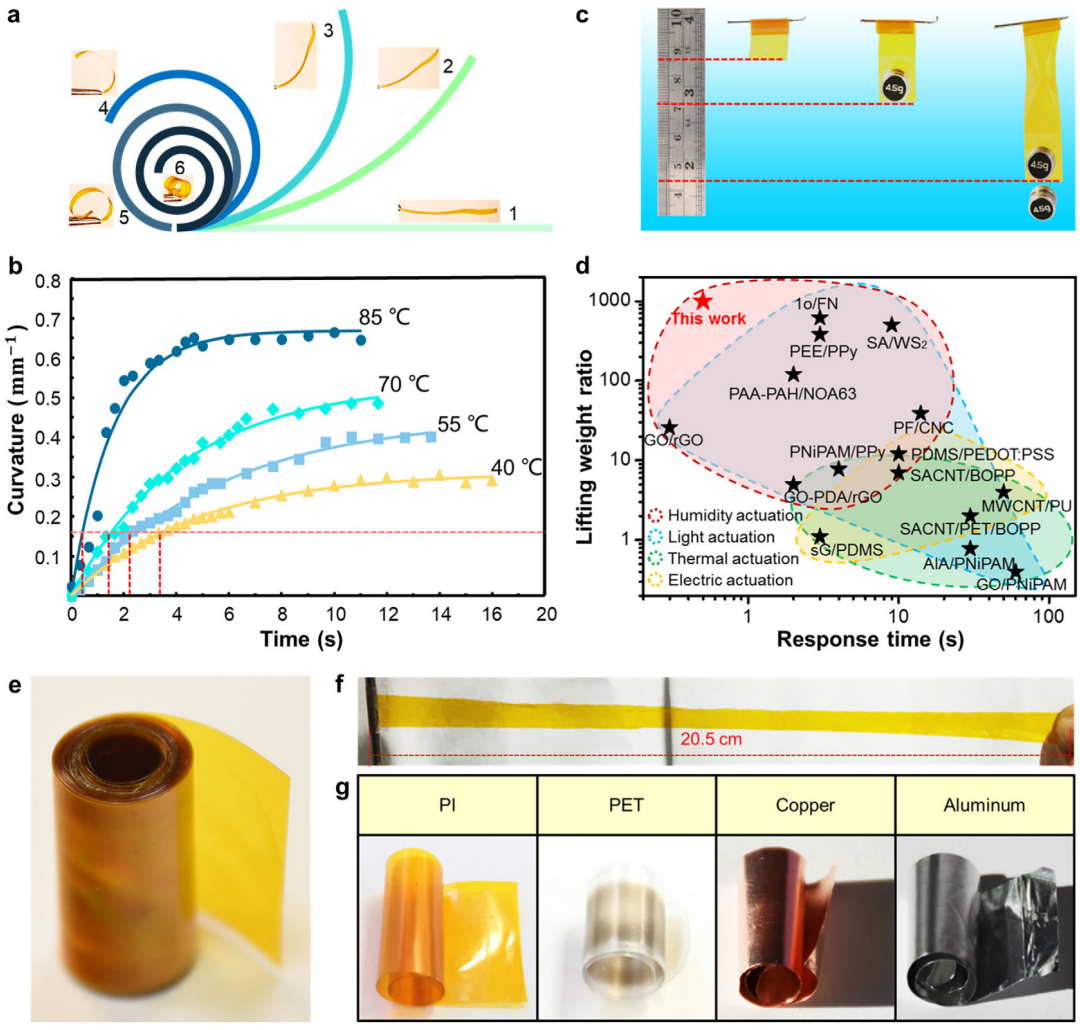

Fig. 3. Stimuli-responsive properties of the CNF-soft actuator. (a) Curling displacement of the CNF-soft actuator during the dehydration process, insets are the corresponding snapshots at different states. (b) Kinetic plots of the CNF-soft actuator driven at various operating temperatures. Solid dots represent the experimental data, solid lines represent the kinetic fitting results, and red dashed lines represent the minimal curvature for the CNF-soft actuator to form a closed loop. (c) Photographs showing a 6 cm × 1 cm × 45 μm sample lifting a 9.0 g weight at 40 °C. (d) Time *vs.* lifting weight ratio plot comparing various stimuli-driven actuators, including: SA/WS_2 [45], PDMS/PEDOT:PSS [29], GO/rGO [46], PAA-PAH/NOA63 [47], AlA/PNiPAM [30], PNiPAM/PPy [48], PF/CNC [31], MWCNT/PU [49], GO/PNiPAM [32], SACNT/PET/BOPP [50], sG/PDMS [33], PEE/PPy [6], 1o/FN [51], GO-PDA/rGO [52], SACNT/BOPP [34]. (e–f) Photographs of a large size (20.5 cm × 1.0 cm × 40 μm) CNF-soft actuator. (g) CNF-soft actuators based on substrates of four different materials (PI, PET, copper and aluminum). (For interpretation of the references to color in this figure legend, the reader is referred to the web version of this article.)

to bend toward the CNF layer, resulting in a closed concentric ring. To quantify the actuation behavior of the CNF-soft actuator, the bending curvature of the strips is plotted against time. Temperature will also significantly influence the water adsorption/desorption behaviors of hygroscopic materials, therefore the bending curvature of the CNF-soft actuator under different temperature is also logged. As expected, at a constant temperature, bending behavior due to desorption of water by the CNF-soft actuator is similar to the swelling behavior of polymers and can be described by a pseudo-first-order kinetic equation [53]. Fitting results precisely overlap the experimental results and suggest pseudo-first-order kinetic behavior of the water desorption process (Fig. 3b, Table S1, and Movie S3). The CNF-soft actuator demonstrates a fast response in 3.3 s at 40 °C, only slightly above body temperature. However, the response time dramatically decreased to approximately 0.5 s when the operating temperature is increased to 85 °C. From these measurements, the rate constant and final curvature for pseudo-first-order behavior increases from 0.21 to 0.63 s^{-1} and 0.31 to 0.67 mm^{-1} with the increase in temperature, respectively. The fast response and large displacement can be ascribed to the multiple parameters impacting the molecular water exchange process including the hygroscopic surface of the cellulose nanofiber, the porosity of the network, and the specially arranged CNFs nanostructure (see details in the modeling discussion part). Moreover, no significantly responsive performance decay was observed after storing the CNF-actuator in air at room temperature for over one year, indicating good durability of the product (Fig. S13).

In addition to the fast response speed and large displacement, the CNF-soft actuator also demonstrates an extremely high lifting capacity. To show the possibility of our CNF-actuator for future application as a soft lift, we prepared a strip of 6 cm × 1 cm × 45 μm actuator. This actuator can easily lift 9.0 g at 45 °C (Fig. 3c), which is nearly 1000 times the weight of the CNFs layer (approximately 250 times the weight of the whole actuator). When compared with literature on diverse stimuli-responsive soft actuators, the response speed and force generated by our CNF-soft actuator are better than most proposed hygroscopic actuators as well

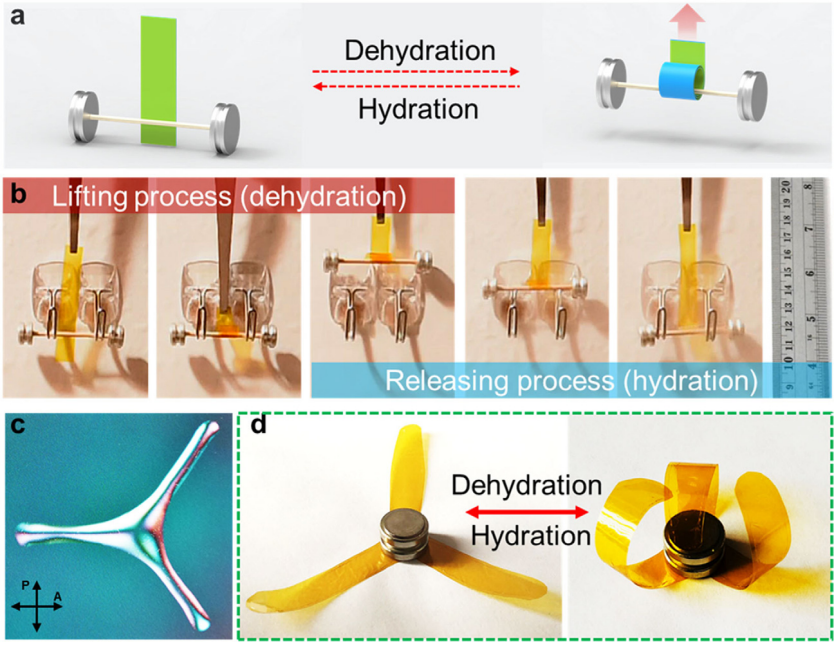

Fig. 4. Proof-of-concept demonstrations as mechanical arms and soft robot. (a) Schematics and (b) photographs illustrating the manipulation of the CNF-soft actuator as a mechanical arm to lift and release the attached object. (c) Polarizing optical image of a trigonal CNF-actuator and (d) its corresponding response behaviors.

as light-driven, thermally driven or electrically driven actuators (Fig. 3d). It is worth to note that our selectively-aligned CNF-soft actuator design also shows good potential towards large-scale production and diverse substrate system. A large sample with 20.5 cm in length and 1.0 cm in width is readily prepared to illustrate the scalability of the CNF-soft actuator (Fig. 3e–f). Moreover, the adaptability of the CNF-soft actuator to different substrates is also verified on both polymer (PI and PET) and metal (copper and aluminum) substrates (Fig. 3g). The excellent stimuli-responsive properties, scalable productivity together with the diverse material system applicability make our selectively aligned CNF-soft actuator appealing for practical application.

2.4. Proof-of-concept demonstration

To further demonstrate the potential applications of our CNF-soft actuator, a 7 cm long CNF-soft actuator is developed to serve as a soft mechanical arm (Fig. 4a–b). Upon heating, the strip executes fast scrolling behavior accompanied by a contraction in length to lift the attached object. By increasing the ambient humidity, unrolling of the strip is observed, resulting in the release of the attached object. In another proof-of-concept application, two ends of the strip are combined to form a wheel-like structure with the CNF layer inside. The wheel-like actuator can roll rapidly under a hot plate or a continuous supply of hot steam (Fig. S14 and Movie S4). This self-walking behavior is ascribed to the combined actions arising from the different transformation of the top and the bottom parts of the wheel-like actuator. The contrasting responses at the top and bottom of the actuator lead to a top-heavy structure and a perpetual motion actuator. A walking speed of 2.1 mm s^{-1} is achieved by this device. Note that the CNF-soft actuator based on the solvent-assisted self-assembly method is not limited to a strip shape. By rationally designing the deposition pattern of the CNF suspension, diverse architecture and complicated movements can also be achieved (Fig. 4c–d), suggesting a great potential of our CNF-actuators for applications in soft robots and biomimetic systems.

2.5. Insights into the responsive properties of the CNF-soft actuator

Mechanics modeling is further carried out to better understand the influence of the selectively aligned CNFs structure on the response properties of the CNF-soft actuator. The loss of moisture content due to water evaporation is accompanied by a decrease in volume of the CNF layer, while the volume of the PI layer remains unchanged. The contraction of the CNF layer on a thin PI substrate introduces differential shrinkage between the two layers. A freestanding CNF/PI bilayer actuator undergoing dehydration bends toward the CNF side to accommodate the deformation and puts the PI layer under tension. When the actuator length is much larger than its width or thickness, the bending deformation due isotropic volumetric strain reduces to a one-dimensional composite beam with two layers. Assuming small bending deformation, this system can be solved analytically [54]. The bending curvature shows a linearly proportional relation to the strain mismatch through Eq. (1) [54–56],

$$\kappa = \left\{ \frac{3E_{\mathrm{PI}}h_{\mathrm{PI}} \cdot E_{\mathrm{CNF}}h_{\mathrm{CNF}} \cdot (h_{\mathrm{PI}} + h_{\mathrm{CNF}})}{(E_{\mathrm{PI}}h_{\mathrm{PI}} + E_{\mathrm{CNF}}h_{\mathrm{CNF}})[E_{\mathrm{PI}}h_{\mathrm{PI}}^2(2h_{PI} + 3h_b) + E_{\mathrm{CNF}}h_{\mathrm{CNF}}^2(2h_{\mathrm{CNF}-3h_b})]} \right\} \Delta\varepsilon_{\mathrm{v}} \tag{1}$$

where E_{PI} (2.5 GPa) and E_{CNF} (20 GPa) are the Young's Moduli of PI and CNF [57], respectively, h_{PI} (30 μm) and h_{CNF} (20 μm) are the thicknesses of each layer, $\Delta\varepsilon_{\mathrm{v}}$ is the shrinkage mismatch, and $h_{\mathrm{b}} = (E_{\mathrm{CNF}}h_{\mathrm{CNF}}^2 - E_{\mathrm{PI}}h_{\mathrm{PI}}^2)/[2(E_{\mathrm{CNF}}h_{\mathrm{CNF}} + E_{\mathrm{PI}}h_{\mathrm{PI}})]$. The volumetric mismatch in Eq. (1) can be approximately determined by the loss of moisture content [58]. In our experiment, $\Delta\varepsilon_{\mathrm{v}}$ varies from a few percents to ten percent (see SI for more simulation details). When the volumetric strain generated due to moisture loss is $\Delta\varepsilon_{\mathrm{v}} > 0.5\%$, the bending deformation exceeds the regime of small strain assumption. The bilayer, furthermore, transforms into a ring, when water in the CNF layer continues to desorb. At this stage, the interlayer interactions start to play a more significant role in the deformation.

To quantify the bending of the CNF-soft actuator under such conditions, a finite element model of a slender stripe with length $L = 50$ mm, width $w = 1$ mm, $h_{\mathrm{PI}} = 30$ μm, and $h_{\mathrm{CNF}} = 20$ μm is

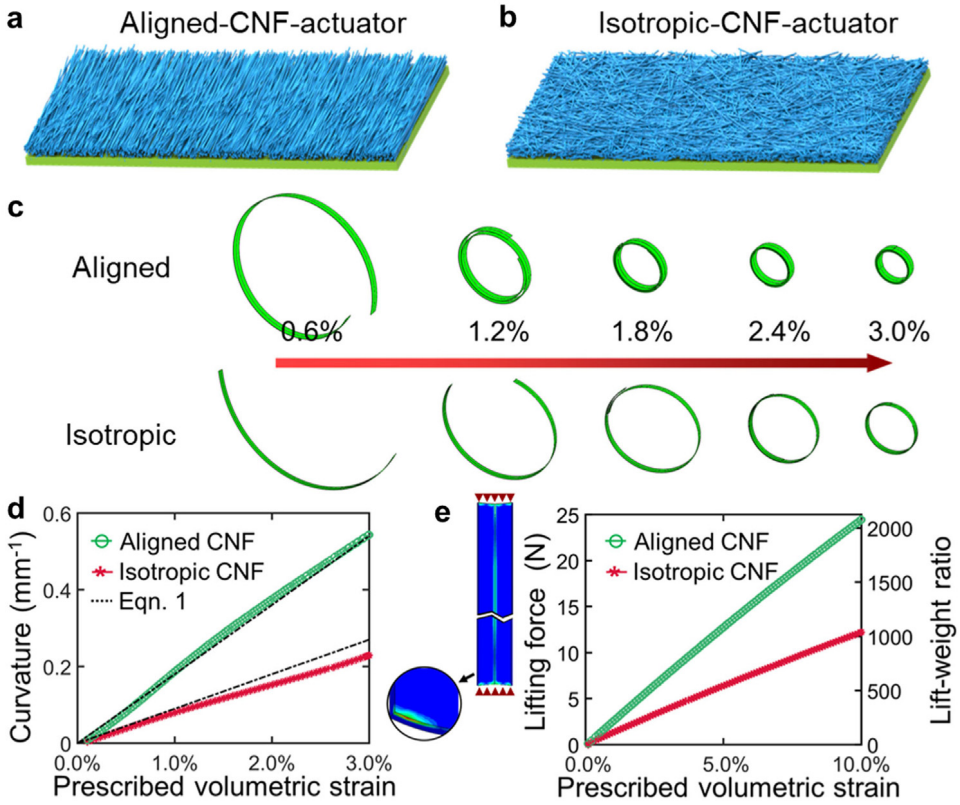

Fig. 5. Mechanics modeling of the effect of fiber alignment on the final curvature and force generated by the CNF-soft actuator. Schematics illustrating the arrangement of (a) selectively aligned-CNF-soft actuator and (b) isotropic-CNF-soft actuator. (c) The shape transformations accompanying the drying processes of aligned-CNF-soft actuator (up) and isotropic-CNF-soft actuator (down), the percentages indicate the volumetric shrinkage of the CNF layer. (d) The curvature of the bilayer scrolls. (e) Intrinsic lifting force generated by the drying effect and the FEM prediction of the lift-weight ratio (Inset: reaction force at the clamped end).

implemented in ABAQUS. The volumetric strain is prescribed by the analogy of thermal expansion. The CNF layer with disordered microscopic arrangement of fibers is modeled as a material with an isotropic coefficient of thermal expansion (CTE) α_{iso} in all directions. Whereas, for aligned-CNF-soft actuator, the CNFs form a highly-ordered structure with fibers oriented in the perpendicular direction to the edges. To simplify the simulation, we assume the moisture only exists between the constituent fibers of the grating-like architecture. Accordingly, when water departs from the CNF layer, the void it leaves will be filled by drawing the parallel fibers closer. Thus, the shrinkage of the oriented CNFs is considered analogous to the thermal expansion behavior of a material with anisotropic CTE so in the direction perpendicular to the fibers, $\alpha_{oriented} = 3\alpha_{iso}$, and in the other two directions $\alpha_2 = \alpha_3 = 0$.

Two types of bilayer structures are modeled: wet CNFs drying without the solvent evaporation induced self-assembly effect, which results in a layer of isotropic CNF bonded to the PI substrate; and wet CNF drying under the influence of the self-assembly effect, which leads to an anisotropic CNF layer on top of the PI substrate (Fig. 5a–b). As shown in Fig. 5c–d, for the isotropic CNF/PI bilayer, the curvature agrees well with the prediction of Eq. 1 for small volume shrinkage. When $\Delta\varepsilon_v > 2\%$, the actual curvature shows an observable deviation from Eq. (1) due to the large deformation and contact between layers [56]. Eq. (1) is only valid in the case where each ply of the bilayer is made of homogeneous material, therefore in order to compare the analytical solution with the FEA model for the oriented CNF bilayer actuator, it is necessary to use an equivalent volumetric strain. The corresponding strain is thus evaluated as an average over the entire active CNF layer, and is weighted respectively by the area of the oriented and the isotropic regime: all the volumetric strain in the oriented CNF regime contributes to the longitudinal contraction, while only 1/3 of volume shrinkage in the isotropic part contributes to the longitudinal contraction. Under such an equivalence, finite element analysis shows good agreement with Eq. (1). For the bilayers drying under the influence of self-assembly effect, the curvature is approximately two times that of the isotropic-CNF-soft actuator.

To quantify the lifting force stemming from the bilayer differential drying, the bilayer actuator is clamped at the two ends to restrain the relative displacement in the longitudinal direction. The reaction force, which is the force required to unwrap the bilayer CNF-soft actuator, is plotted in Fig. 5e, which increases linearly with the volumetric strain. The reaction force is doubled when accounting for partial alignment due to the self-assembly effect. The mass of the CNF layer and the reaction force also determine the lifting-weight ratio, assuming $\rho_{CNF} = 1.2\ g\ cm^{-3}$ [57]. Accordingly, a lift-weight ratio of 1000 can be achieved by the selectively aligned CNF-soft actuator at a prescribed volumetric strain of 5%, which is ~2 times that of the isotropic-CNF-soft actuator. Moreover, the lift-weight ratio of the selectively aligned CNF-soft actuator can be further increased when a stronger stimulus (i.e. more volumetric strain) is applied.

3. Conclusions

In summary, we design a micro-patterned soft actuator with selectively aligned CNFs on top of a passivation substrate. The unique arrangement of CNF is achieved by a facile evaporation-assisted self-assembly method. The selectively aligned CNF network can fast exchange water molecules with the external

environment, enabling rapid actuation responses from the resultant CNF-soft actuator. Finite element analysis shows that the selectively aligned CNF layer determines both the direction and generation of the actuation force. Compared with conventional bilayer soft actuator with isotropic active layer, the selectively aligned CNF layer in our design endows fast (response time less than 1 s), powerful (1000 times of its self-weight), and well-controlled deformations. Micro-patterned CNF-soft actuators build on various substrates further confirmed the versatility of the self-assembly method for a range of material systems. Demonstrations of the resultant CNF-soft actuator as load-bearing mechanical arms and soft walking robots suggest numerous potential applications of CNF-soft actuators in field of soft robots and biomimetic systems.

Experimental methods

Preparation of CNFs. 0.7 wt% TEMPO-oxidized pulp from a commercial bleached softwood pulp was obtained by the same method as mentioned in our previous study [59]. The TEMPO-oxidized pulp was thoroughly washed to remove residual salt, and ultrasonicated at 60% power for 60 mins to prepare the 0.7 wt% CNF suspension. The CNF suspension is used right immediately after preparation due to the eventual increase in viscosity caused by suspension gelation.

Fabrication of the CNF-soft actuator. A certain amount of the fresh prepared 0.7 wt% CNF suspension was poured on the passive substrate. The substrate was mounted on a glass slide to prevent drying-induced deformation. The samples were placed in a humidity chamber at a constant temperature of 25 °C and a relative humidity of 50%. The whole drying process was performed in a stable environment until the CNF suspension was completely dry. CNF-soft actuator was obtained by peeling off from the glass slides and trimming to size.

Characterizations. The morphology and structure of the CNF-soft actuator were characterized by scanning electron microscopy (SEM, Hitachi SU-70). The morphology of the cellulose nanofibers was obtained utilizing an Atomic Force Microscope (AFM, Bruker Multimode 8) in tapping mode. FT-IR spectrum was carried out on a Thermo Nicolet NEXUS 670 FTIR ranging from 600 to 4000 cm^{-1} under ATR mode.

Acknowledgments

We acknowledge the support of the Maryland NanoCenter and its AIMLab. Yudi Kuang acknowledges the financial support of China Scholarship Council (201606150041). Teng Li and Jian Cheng acknowledge the financial support of NASA, United States (Grant number: NNX12AM02G).

Appendix A. Supplementary data

Supplementary material related to this article can be found online at https://doi.org/10.1016/j.eml.2019.100463.

References

[1] E.T. Roche, R. Wohlfarth, J.T. Overvelde, N.V. Vasilyev, F.A. Pigula, D.J. Mooney, K. Bertoldi, C.J. Walsh, A bioinspired soft actuated material, Adv. Mater. 26 (2014) 1200–1206, http://dx.doi.org/10.1002/adma.201304018.

[2] K. Lee, S. Tawfick, Fiber micro-architected electro–elasto-kinematic muscles, Extreme Mech. Lett. 8 (2016) 64–69, http://dx.doi.org/10.1016/j.eml.2016.03.003.

[3] Y. Wang, J. Zhu, Artificial muscles for jaw movements, Extreme Mech. Lett. 6 (2016) 88–95, http://dx.doi.org/10.1016/j.eml.2015.12.007.

[4] D. Rus, M.T. Tolley, Design, fabrication and control of soft robots, Nature 521 (2015) 467–475, http://dx.doi.org/10.1038/nature14543.

[5] R.V. Martinez, A.C. Glavan, C. Keplinger, A.I. Oyetibo, G.M. Whitesides, Soft actuators and robots that are resistant to mechanical damage, Adv. Funct. Mater. 24 (2014) 3003–3010, http://dx.doi.org/10.1002/adfm.201303676.

[6] M. Ma, L. Guo, D.G. Anderson, R. Langer, Bio-inspired polymer composite actuator and generator driven by water gradients, Science 339 (2013) 186–189, http://dx.doi.org/10.1126/science.1230262.

[7] E. Bortot, M. Gei, Harvesting energy with load-driven dielectric elastomer annular membranes deforming out-of-plane, Extreme Mech. Lett. 5 (2015) 62–73, http://dx.doi.org/10.1016/j.eml.2015.09.009.

[8] D. Peter, R. Pichler, S. Bauer, R. Schwödiauer, Electrostatic converter with an electret-like elastomer membrane for large scale energy harvesting of low density energy sources, Extreme Mech. Lett. 4 (2015) 38–44, http://dx.doi.org/10.1016/j.eml.2015.07.008.

[9] R.F. Shepherd, F. Ilievski, W. Choi, S.A. Morin, A.A. Stokes, A.D. Mazzeo, X. Chen, M. Wang, G.M. Whitesides, Multigait soft robot, Proc. Natl. Acad. Sci. 108 (2011) 20400–20403, http://dx.doi.org/10.1073/pnas.1116564108.

[10] F. Ilievski, A.D. Mazzeo, R.F. Shepherd, X. Chen, G.M. Whitesides, Soft robotics for chemists, Angew. Chem. 123 (2011) 1930–1935, http://dx.doi.org/10.1002/ange.201006464.

[11] L. Romasanta, M. Lopez-Manchado, R. Verdejo, Increasing the performance of dielectric elastomer actuators: A review from the materials perspective, Prog. Polym. Sci. 51 (2015) 188–211, http://dx.doi.org/10.1016/j.progpolymsci.2015.08.002.

[12] R.H. Baughman, C. Cui, A.A. Zakhidov, Z. Iqbal, J.N. Barisci, G.M. Spinks, G.G. Wallace, A. Mazzoldi, D. De Rossi, A.G. Rinzler, Carbon nanotube actuators, Science 284 (1999) 1340–1344, http://dx.doi.org/10.1126/science.284.5418.1340.

[13] R. Pelrine, R. Kornbluh, Q. Pei, J. Joseph, High-speed electrically actuated elastomers with strain greater than 100%, Science 287 (2000) 836–839, http://dx.doi.org/10.1126/science.287.5454.836.

[14] T. Lu, Z. Shi, Q. Shi, T. Wang, Bioinspired bicipital muscle with fiber-constrained dielectric elastomer actuator, Extreme Mech. Lett. 6 (2016) 75–81, http://dx.doi.org/10.1016/j.eml.2015.12.008.

[15] Y.S. Teh, S.J.A. Koh, Giant continuously-tunable actuation of a dielectric elastomer ring actuator, Extreme Mech. Lett. 9 (2016) 195–203, http://dx.doi.org/10.1016/j.eml.2016.07.002.

[16] U. Gupta, H. Godaba, Z. Zhao, C.K. Chui, J. Zhu, Tunable force/displacement of a vibration shaker driven by a dielectric elastomer actuator, Extreme Mech. Lett. 2 (2015) 72–77, http://dx.doi.org/10.1016/j.eml.2015.02.004.

[17] J. Cheng, Z. Jia, T. Li, Dielectric-elastomer-based capacitive force sensing with tunable and enhanced sensitivity, Extreme Mech. Lett. 21 (2018) 49–56, http://dx.doi.org/10.1016/j.eml.2018.03.004.

[18] C. Wang, Y. Wang, Y. Yao, W. Luo, J. Wan, J. Dai, E. Hitz, K.K. Fu, L. Hu, A solution-processed high-temperature, flexible, thin-film actuator, Adv. Mater. 28 (2016) 8618–8624, http://dx.doi.org/10.1002/adma.201602777.

[19] J. Wang, Z. Chen, M. Mauk, K.-S. Hong, M. Li, S. Yang, H.H. Bau, Self-actuated, thermo-responsive hydrogel valves for lab on a chip, Biomed. Microdevices 7 (2005) 313–322, http://dx.doi.org/10.1007/s10544-005-6073-z.

[20] M.C. LeMieux, M.E. McConney, Y.-H. Lin, S. Singamaneni, H. Jiang, T.J. Bunning, V.V. Tsukruk, Polymeric nanolayers as actuators for ultrasensitive thermal bimorphs, Nano Lett. 6 (2006) 730–734, http://dx.doi.org/10.1021/nl0525305.

[21] H. Guo, J. Cheng, J. Wang, P. Huang, Y. Liu, Z. Jia, X. Chen, K. Sui, T. Li, Z. Nie, Reprogrammable ultra-fast shape-transformation of macroporous composite hydrogel sheets, J. Mater. Chem. B 5 (2017) 2883–2887, http://dx.doi.org/10.1039/C6TB02198K.

[22] K. Kumar, C. Knie, D. Bléger, M.A. Peletier, H. Friedrich, S. Hecht, D.J. Broer, M.G. Debije, A.P. Schenning, A chaotic self-oscillating sunlight-driven polymer actuator, Nature Commun. 7 (2016) http://dx.doi.org/10.1038/ncomms11975.

[23] A.A. Skandani, S. Chatterjee, M.L. Smith, J. Baranski, D.H. Wang, L.-S. Tan, T.J. White, M.R. Shankar, Discrete-state photomechanical actuators, Extreme Mech. Lett. 9 (2016) 45–54, http://dx.doi.org/10.1016/j.eml.2016.05.002.

[24] X. Wang, B. Han, R.-P. Yu, F.-C. Li, Z.-Y. Zhao, Q.-C. Zhang, T.J. Lu, Magnetic-responsive Fe_3O_4 nanoparticle-impregnated cellulose paper actuators, Extreme Mech. Lett. 25 (2018) 53–59, http://dx.doi.org/10.1016/j.eml.2018.10.003.

[25] Q. Zhao, J. Heyda, J. Dzubiella, K. Täuber, J.W. Dunlop, J. Yuan, Sensing solvents with ultrasensitive porous poly (ionic liquid) actuators, Adv. Mater. 27 (2015) 2913–2917, http://dx.doi.org/10.1002/adma.201500533.

[26] P. Chen, Y. Xu, S. He, X. Sun, S. Pan, J. Deng, D. Chen, H. Peng, Hierarchically arranged helical fibre actuators driven by solvents and vapours, Nature Nanotechnol. (2015) http://dx.doi.org/10.1038/nnano.2015.198.

[27] T. Xu, Q. Han, Z. Cheng, J. Zhang, L. Qu, Interactions between graphene-based materials and water molecules toward actuator and electricity-generator applications, Small Methods 2 (2018) 180010, http://dx.doi.org/10.1002/smtd.2018001088.

[28] D.E. Hagaman, S. Leist, J. Zhou, H.-F. Ji, Photoactivated polymeric bilayer actuators fabricated via 3D printing, ACS Appl. Mater. Interfaces 10 (2018) 27308–27315, http://dx.doi.org/10.1021/acsami.8b08503.
[29] S. Taccola, F. Greco, E. Sinibaldi, A. Mondini, B. Mazzolai, V. Mattoli, Toward a new generation of electrically controllable hygromorphic soft actuators, Adv. Mater. 27 (2015) 1668–1675, http://dx.doi.org/10.1002/adma.201404772.
[30] W.J. Zheng, N. An, J.H. Yang, J. Zhou, Y.M. Chen, Tough al-alginate/poly (n-isopropylacrylamide) hydrogel with tunable lcst for soft robotics, ACS Appl. Mater. Interfaces 7 (2015) 1758–1764, http://dx.doi.org/10.1021/am507339r.
[31] M.K. Khan, W.Y. Hamad, M.J. MacLachlan, Tunable mesoporous bilayer photonic resins with chiral nematic structures and actuator properties, Adv. Mater. 26 (2014) 2323–2328, http://dx.doi.org/10.1002/adma.201304966.
[32] E. Zhang, T. Wang, W. Hong, W. Sun, X. Liu, Z. Tong, Infrared-driving actuation based on bilayer graphene oxide-poly (N-isopropylacrylamide) nanocomposite hydrogels, J. Mater. Chem. A 2 (2014) 15633–15639, http://dx.doi.org/10.1039/C4TA02866J.
[33] Y. Hu, T. Lan, G. Wu, Z. Zhu, W. Chen, A spongy graphene based bimorph actuator with ultra-large displacement towards biomimetic application, Nanoscale 6 (2014) 12703–12709, http://dx.doi.org/10.1039/C4NR02768J.
[34] L. Chen, M. Weng, Z. Zhou, Y. Zhou, L. Zhang, J. Li, Z. Huang, W. Zhang, C. Liu, S. Fan, Large-deformation curling actuators based on carbon nanotube composite: Advanced-structure design and biomimetic application, ACS Nano 9 (2015) 12189–12196, http://dx.doi.org/10.1021/acsnano.5b05413.
[35] P. Fratzl, F.G. Barth, Biomaterial systems for mechanosensing and actuation, Nature 462 (2009) 442–448, http://dx.doi.org/10.1038/nature08603.
[36] A.R. Studart, Biologically inspired dynamic material systems, Angew. Chemie Int. Ed. 54 (2015) 3400–3416, http://dx.doi.org/10.1002/anie.201410139.
[37] I. Burgert, P. Fratzl, Actuation systems in plants as prototypes for bioinspired devices, Philos. Trans. R. Soc. Lond. Ser. A Math. Phys. Eng. Sci. 367 (2009) 1541–1557, http://dx.doi.org/10.1098/rsta.2009.0003.
[38] L.T. de Haan, J.M. Verjans, D.J. Broer, C.W. Bastiaansen, A.P. Schenning, Humidity-responsive liquid crystalline polymer actuators with an asymmetry in the molecular trigger that bend, fold, and curl, J. Am. Chem. Soc. 136 (2014) 10585–10588, http://dx.doi.org/10.1021/ja505475x.
[39] J. Deng, J. Li, P. Chen, X. Fang, X. Sun, Y. Jiang, W. Weng, B. Wang, H. Peng, Tunable photothermal actuators based on a pre-programmed aligned nanostructure, J. Am. Chem. Soc. (2015) http://dx.doi.org/10.1021/jacs.5b10131.
[40] L. Zhang, S. Chizhik, Y. Wen, P. Naumov, Directed motility of hygroresponsive biomimetic actuators, Adv. Funct. Mater. 26 (2016) 1040–1053, http://dx.doi.org/10.1002/adfm.201503922.
[41] L. Liu, S. Jiang, Y. Sun, S. Agarwal, Giving direction to motion and surface with ultra-fast speed using oriented hydrogel fibers, Adv. Funct. Mater. (2015) http://dx.doi.org/10.1002/adfm.201503612.
[42] D.D. Han, Y.L. Zhang, Y. Liu, Y.Q. Liu, H.B. Jiang, B. Han, X.Y. Fu, H. Ding, H.L. Xu, H.B. Sun, Bioinspired graphene actuators prepared by unilateral UV irradiation of graphene oxide papers, Adv. Funct. Mater. 25 (2015) 4548–4557, http://dx.doi.org/10.1002/adfm.201501511.
[43] S. Liu, E. Boatti, K. Bertoldi, R. Kramer-Bottiglio, Stimuli-induced bidirectional hydrogel unimorph actuators, Extreme Mech. Lett. 21 (2018) 35–43, http://dx.doi.org/10.1016/j.eml.2018.03.001.
[44] M. Kuang, L. Wang, Y. Song, Controllable printing droplets for high-resolution patterns, Adv. Mater. 26 (2014) 6950–6958, http://dx.doi.org/10.1002/adma.201305416.
[45] L. Zong, M. Li, C. Li, Bioinspired coupling of inorganic layered nanomaterials with marine polysaccharides for efficient aqueous exfoliation and smart actuating hybrids, Adv. Mater. (2017) http://dx.doi.org/10.1002/adma.201604691.
[46] J. Mu, C. Hou, B. Zhu, H. Wang, Y. Li, Q. Zhang, A multi-responsive water-driven actuator with instant and powerful performance for versatile applications, Sci. Rep. 5 (2015) http://dx.doi.org/10.1038/srep09503.
[47] Y. Ma, Y. Zhang, B. Wu, W. Sun, Z. Li, J. Sun, Polyelectrolyte multilayer films for building energetic walking devices, Angew. Chem. 123 (2011) 6378–6381, http://dx.doi.org/10.1002/ange.201101054.
[48] R. Luo, J. Wu, N.D. Dinh, C.H. Chen, Gradient porous elastic hydrogels with shape-memory property and anisotropic responses for programmable locomotion, Adv. Funct. Mater. 25 (2015) 7272–7279, http://dx.doi.org/10.1002/adfm.201503434.
[49] Z. Zeng, H. Jin, L. Zhang, H. Zhang, Z. Chen, F. Gao, Z. Zhang, Low-voltage and high-performance electrothermal actuator based on multi-walled carbon nanotube/polymer composites, Carbon 84 (2015) 327–334, http://dx.doi.org/10.1016/j.carbon.2014.12.012.
[50] L. Chen, M. Weng, W. Zhang, Z. Zhou, Y. Zhou, D. Xia, J. Li, Z. Huang, C. Liu, S. Fan, Transparent actuators and robots based on single-layer superaligned carbon nanotube sheet and polymer composites, Nanoscale 8 (2016) 6877–6883, http://dx.doi.org/10.1039/C5NR07237A.
[51] M. Morimoto, M. Irie, A diarylethene cocrystal that converts light into mechanical work, J. Am. Chem. Soc. 132 (2010) 14172–14178, http://dx.doi.org/10.1021/ja105356w.
[52] J. Mu, C. Hou, H. Wang, Y. Li, Q. Zhang, M. Zhu, Origami-inspired active graphene-based paper for programmable instant self-folding walking devices, Sci. Adv. 1 (2015) e150053, http://dx.doi.org/10.1126/sciadv.15005333.
[53] Z. Fang, Y. Kuang, P. Zhou, S. Ming, P. Zhu, Y. Liu, H. Ning, G. Chen, Programmable shape recovery process of water-responsive shape-memory poly (vinyl alcohol) by wettability contrast strategy, ACS Appl. Mater. Interfaces 9 (2017) 5495–5502, http://dx.doi.org/10.1021/acsami.6b14868.
[54] S. Timoshenko, Analysis of bi-metal thermostats, J. Opt. Soc. Amer. 11 (1925) 233–255.
[55] C. Hsueh, S. Lee, T.J. Chuang, An alternative method of solving multilayer bending problems, Trans.-Am. Soc. Mech. Eng. J. Appl. Mech. 70 (2003) 151–153, http://dx.doi.org/10.1115/1.1526123.
[56] L. Freund, J. Floro, E. Chason, Extensions of the Stoney formula for substrate curvature to configurations with thin substrates or large deformations, Appl. Phys. Lett. 74 (1999) 1987–1989, http://dx.doi.org/10.1063/1.123722.
[57] H. Zhu, S. Zhu, Z. Jia, S. Parvinian, Y. Li, O. Vaaland, L. Hu, T. Li, Anomalous scaling law of strength and toughness of cellulose nanopaper, Proc. Natl. Acad. Sci. 112 (2015) 8971–8976, http://dx.doi.org/10.1073/pnas.1502870112.
[58] A. Hailwood, S. Horrobin, Absorption of water by polymers: analysis in terms of a simple model, Trans. Faraday Soc. 42 (1946) B084–B092, http://dx.doi.org/10.1039/TF946420B084.
[59] Y. Kuang, G. Chen, S. Ming, Z. Wu, Z. Fang, Solvent resistance of 2, 2, 6, 6-tetramethylpiperidine-1-oxyl (TEMPO) treated cellulose nanofiber film for flexible electronics, Cellulose 23 (2016) 1979–1987, http://dx.doi.org/10.1007/s10570-016-0906-1.

Supporting Information

Selectively Aligned Cellulose Nanofibers Towards High-Performance Soft Actuators

Yudi Kuang[1,2,4], Chaoji Chen[2,4], Jian Cheng[3,4], Glenn Pastel[2], Tian Li[2], Jianwei Song[2], Feng Jiang[2], Yiju Li[2], Ying Zhang[2], Soo-Hwan Jang[2], Gang Chen[1], Teng Li[3,*], Liangbing Hu[2,*]

[1]State Key Laboratory of Pulp and Paper Engineering, South China University of Technology, Guangzhou, 510640
[2]Department of Materials Science and Engineering, University of Maryland, College Park, Maryland, 20742
[3]Department of Mechanical Engineering, University of Maryland, College Park, Maryland, 20742
[4]These authors contributed equally to this work.

*Correspondence: binghu@umd.edu (Liangbing Hu); lit@umd.edu (Teng Li)

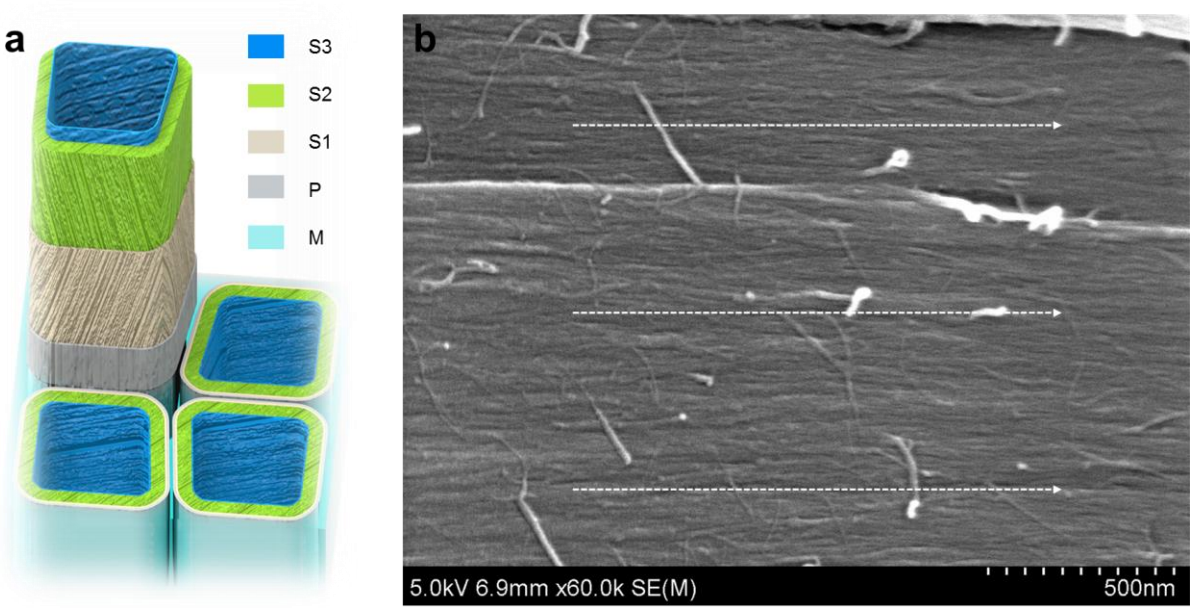

Fig. S1. The naturally aligned cellulose nanofibers (CNFs) in the wood fiber. (a) Schematic showing the directional alignment of CNFs in the layers of wood fiber. (b) SEM image showing the aligned CNFs in the S3 layer of the wood fiber.

Fig. S2. Photographs depicting the preparation of the CNF suspension. The clear and transparent appearance of the resultant solution indicating a good dispersion of the nano-sized cellulose fibrils.

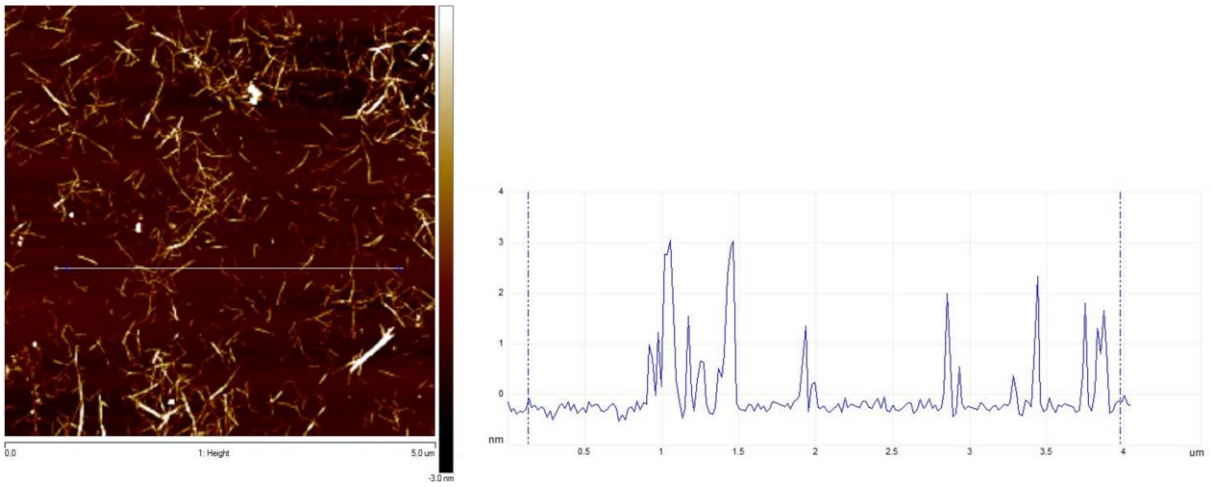

Fig. S3. AFM image (left panel) showing the morphology of the resulted CNFs by spray coating and drying the 0.05 wt% CNF solution on top of the mica at 105 °C. The right panel is the height plotting of the cutting line in the AFM image, showing that the diameter of the cellulose nanofiber is approximately 1~3 nm.

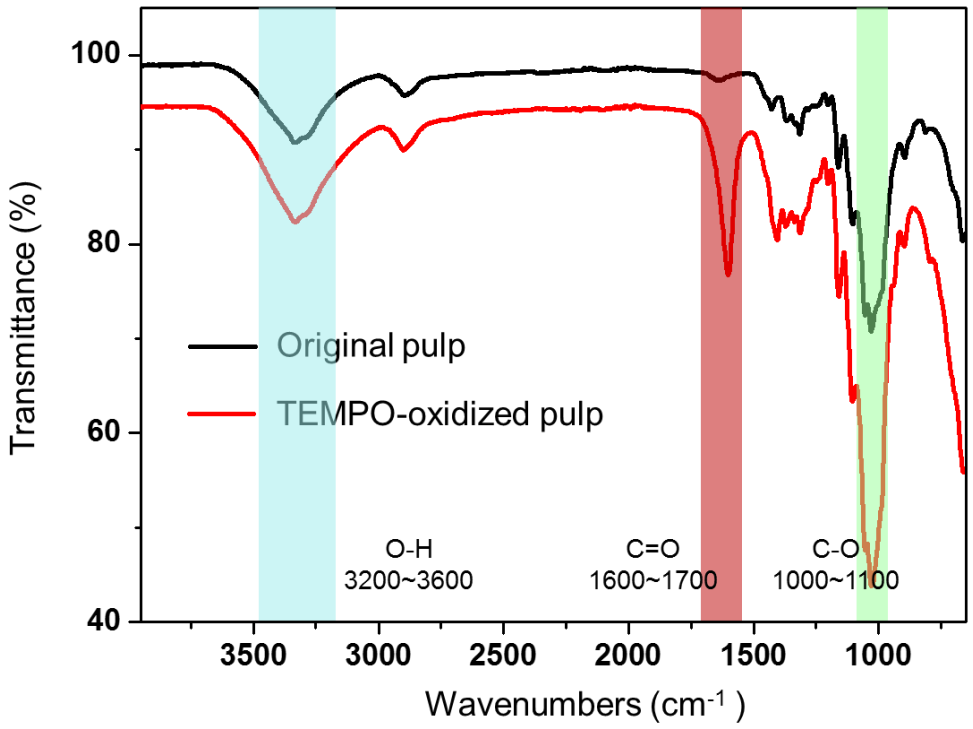

Fig. S4. FI-IR plot of the TEMPO-oxidized cellulose. The peak around 3400 cm^{-1} and 1650 cm^{-1} are the O-H and C=O stretch vibration absorption, respectively, indicating the hydroxyl groups at the C-6 have successfully oxidized to carboxyl groups.

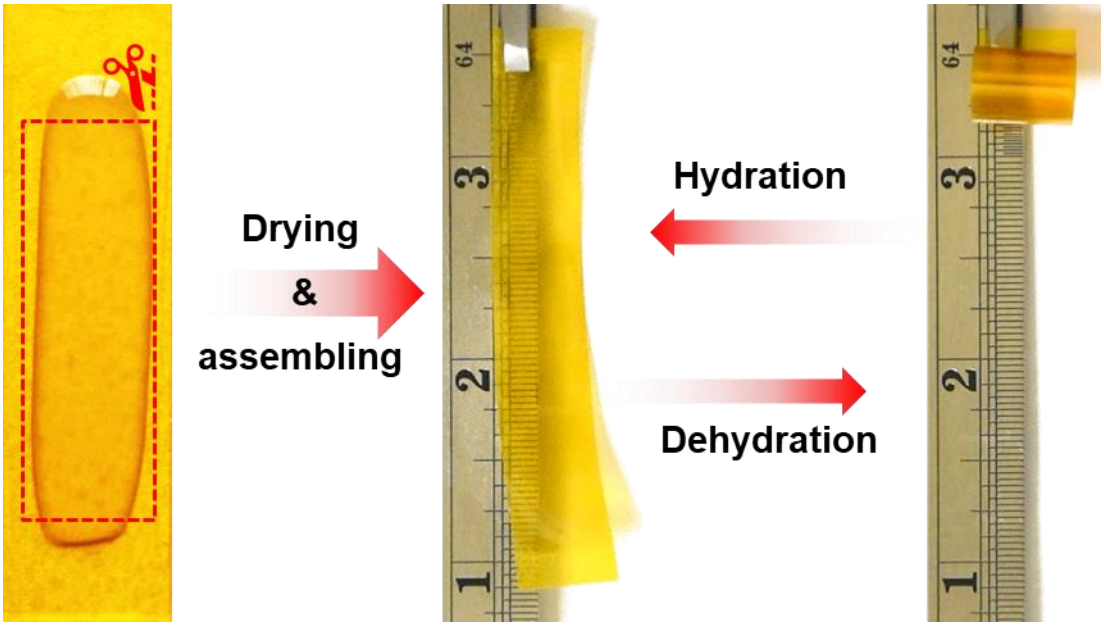

Fig. S5. Photographs showing the fabrication and actuation of the CNF-soft actuator.

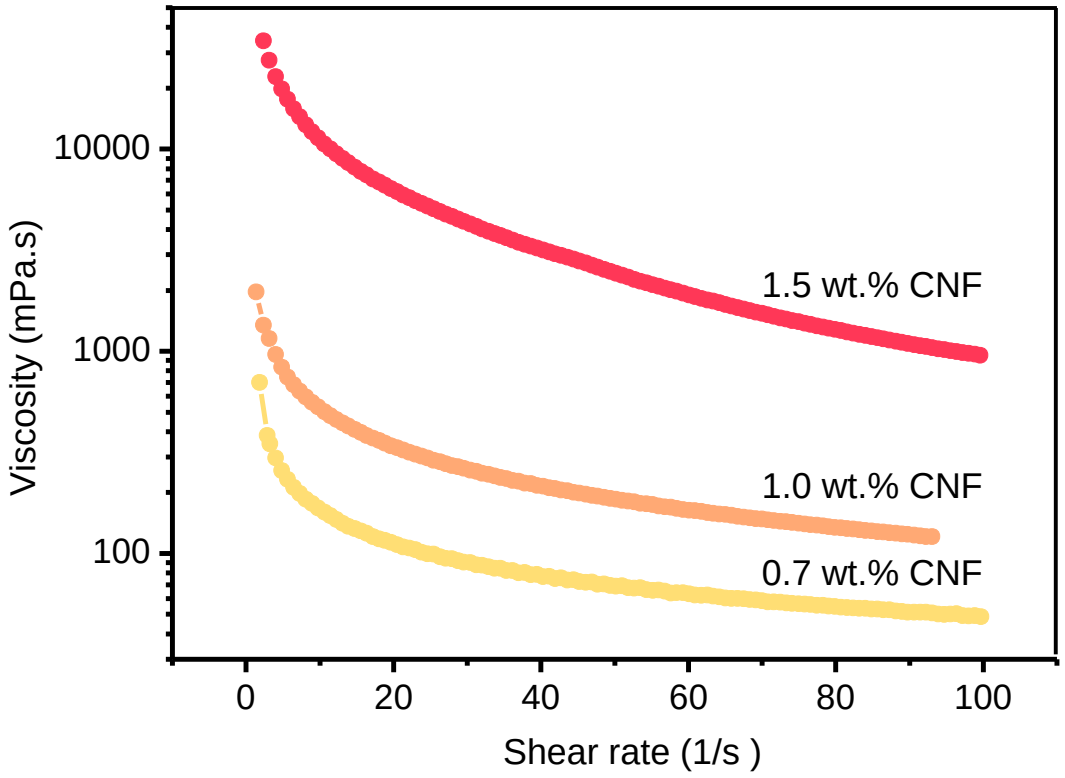

Fig. S6. The viscosity vs. shear rate plots of the CNF suspensions with different concetration 0.7 wt.%, 1.0 wt.%, and 1.5wt.%, respectively.

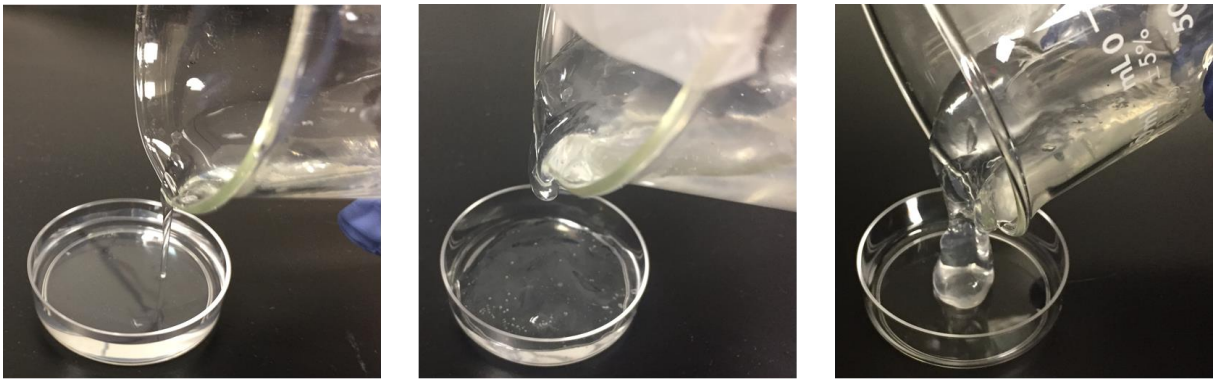

0.7 wt.% 1.0 wt.% 1.5 wt.%

Fig. S7. Photographs showing the significant viscosity change of the CNF suspension at different concetrations, 0.7 wt.%, 1.0 wt.%, and 1.5wt.%, respectively. CNF solution demonstrates very good flowability at a concentration of 0.7 wt.%, enabling the orientation of CNF due to the convection flow in the casting solution. The oriented CNF state will be maintained during the drying-induced gelation process, resulting in an anisotropic CNF deposition.

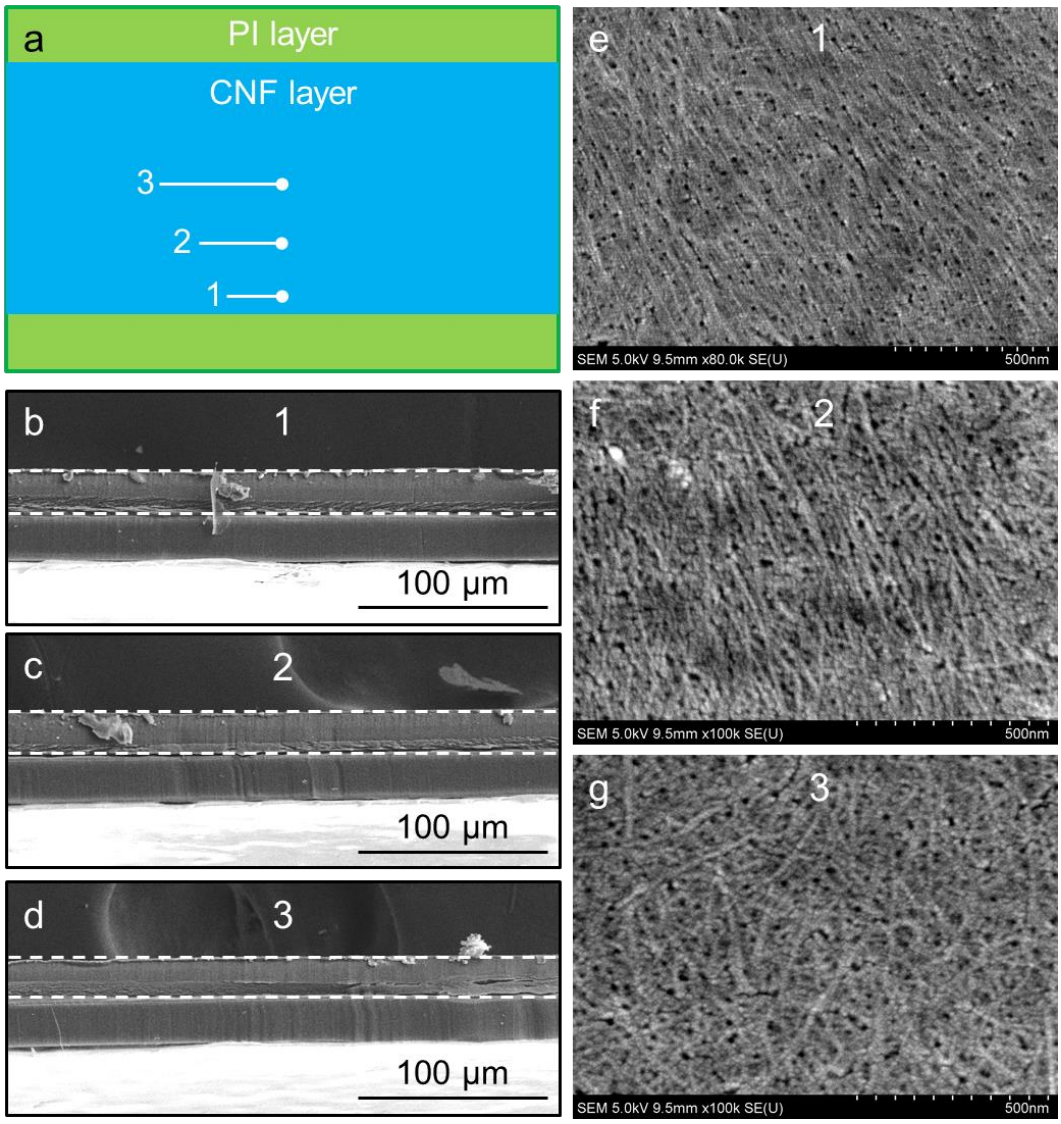

Fig. S8. Morphology characterization of the CNF deposition layer. (a) Schematic illustrating the observation area of the CNF deposition. (b-d) Side-view SEM images of the corresponding areas marked in (a), and (e-g) are the corresponding top-view SEM images showing the alignment of the CNFs.

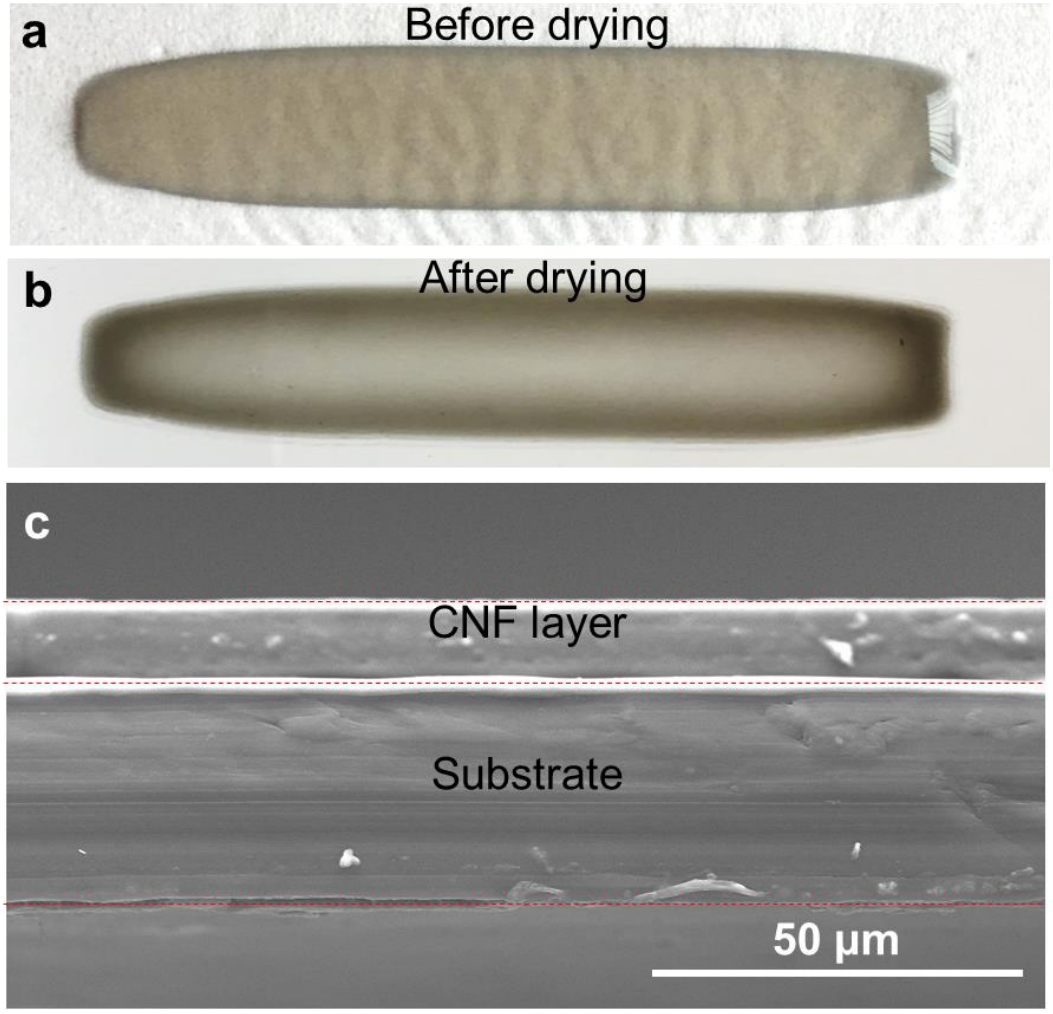

Fig. S9. Photograph images showing the solvent-assisted self-assembly pattern of the CNF solution with 5 wt% CNT as visible tracer (a) before and (b) after drying. A clear dark region caused by the enrichment of CNT is observed along the perimeter of the deposition, indicating the existence of the capillary flow during the drying process. (c) SEM image illustrating uniform deposition of the CNF layer with a thickness around 10 μm.

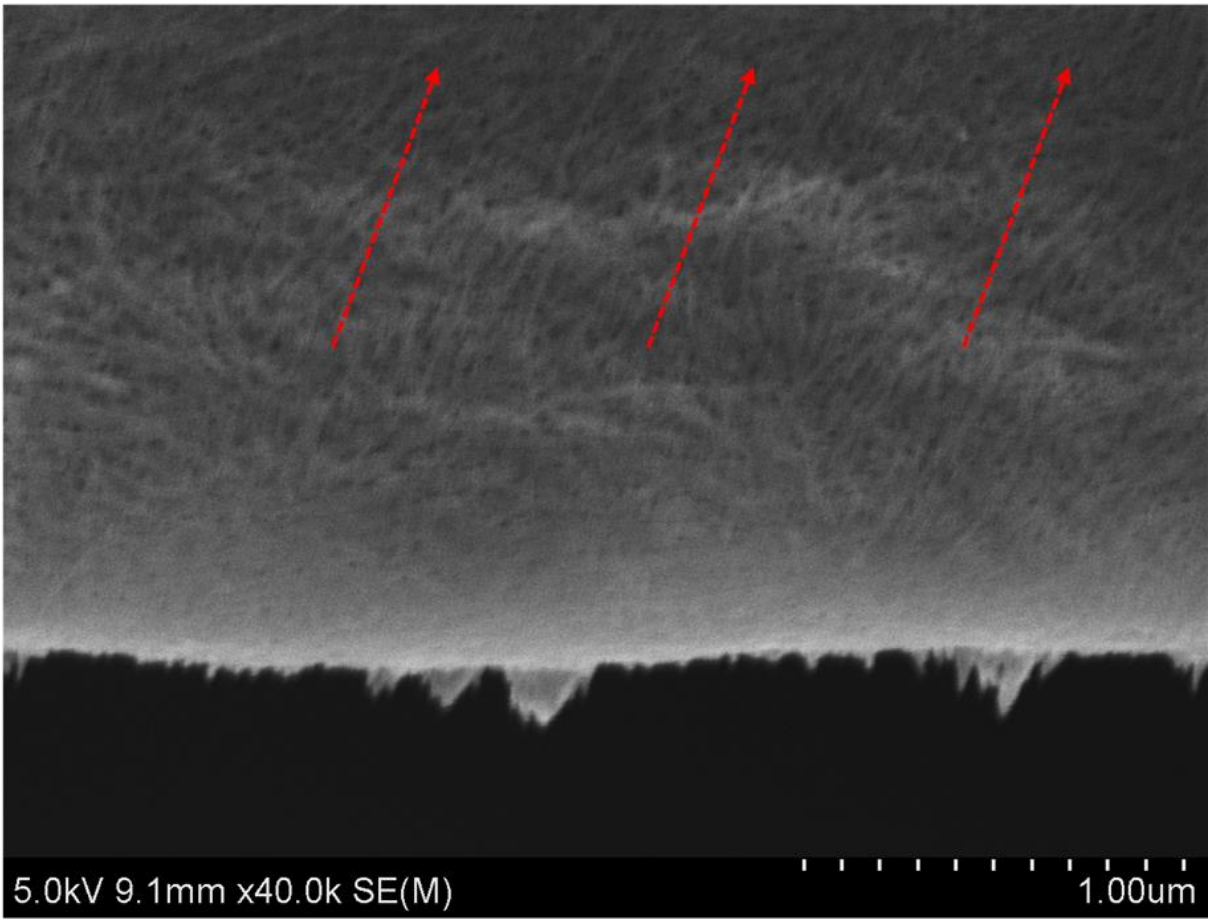

Fig. S10. SEM image showing the CNFs perpendicularly aligned to the perimeter.

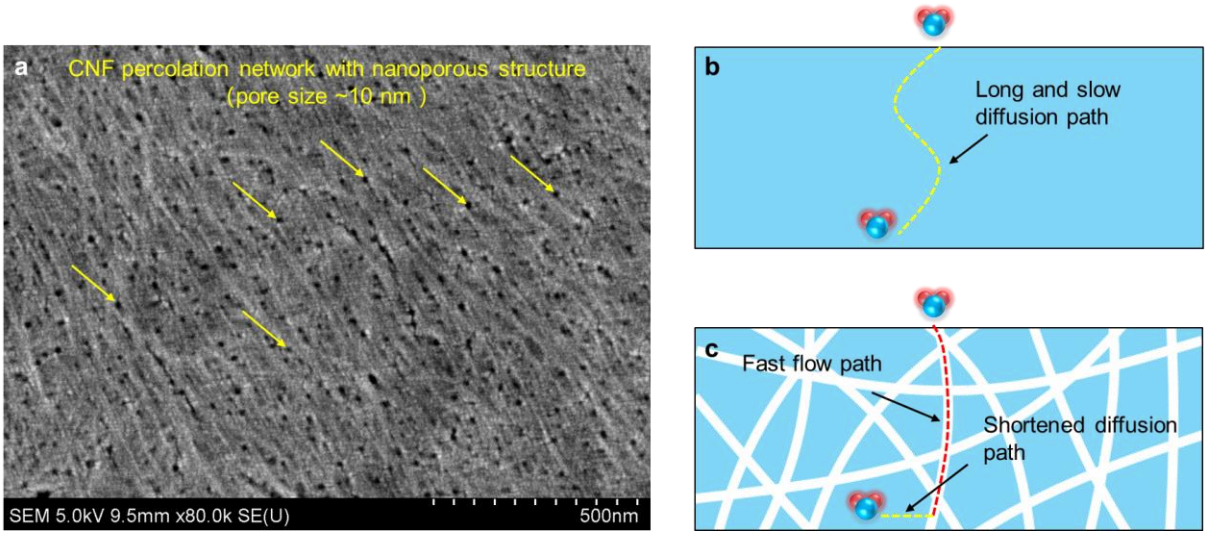

Fig. S11. (a) SEM image of the percolation network formed by the CNFs and the corresponding naturally formed nanopores. (b-c) Schematics illustrating the interconnected pores on the influence of water molecular absorption/desorption processes.

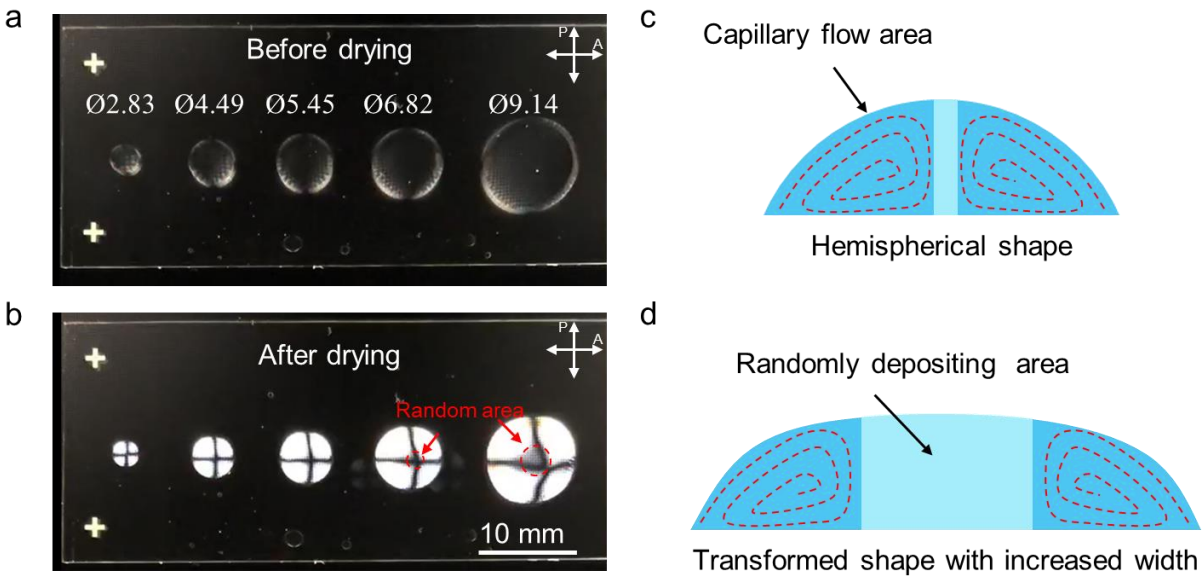

Fig. S12. POM images of the CNF droplets with different diameters (a) before and (b) after drying. (c-d) Schematics illustrating the geometric limit on the assembly behavior of the CNF droplet.

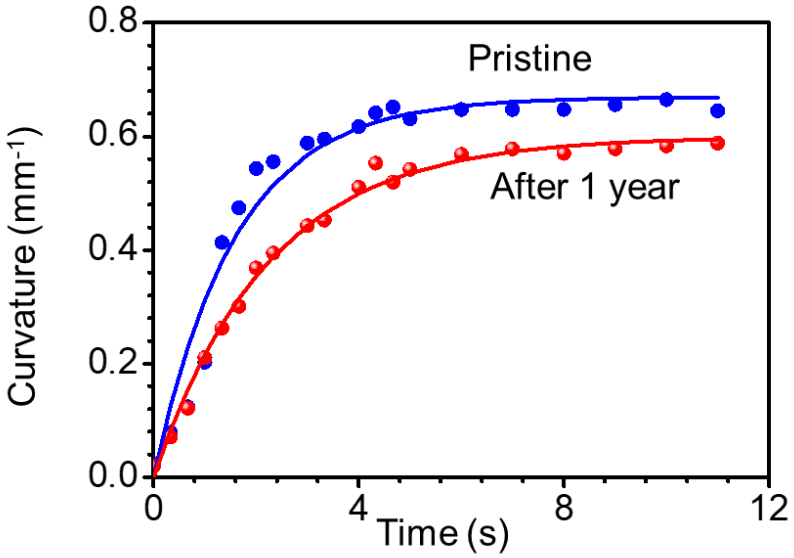

Fig. S13. Responsive property of the CNF actuator before and after storing in air for over 1 year. The testing temperature is 85 °C.

Table S1. The pseudo first order kinetic fitting results of the CNF-soft actuator at different temperature

Sample	q_e (mm^{-1})	k_1 (s^{-1})	R^2
40	0.3122	0.2096	0.9953
55	0.4547	0.1744	0.9943
70	0.5374	0.2321	0.9934
85	0.6692	0.6286	0.9608

According to the pseudo-first-order kinetic model, the kinetic equation of the CNF-soft actuator can be expressed as

$$q_t = q_e - q_e e^{-k_1 t}$$

where q_e and q_t (mm^{-1}) are the curvature at equilibrium and at time t, respectively. k_1(s^{-1}) is the kinetic constant.

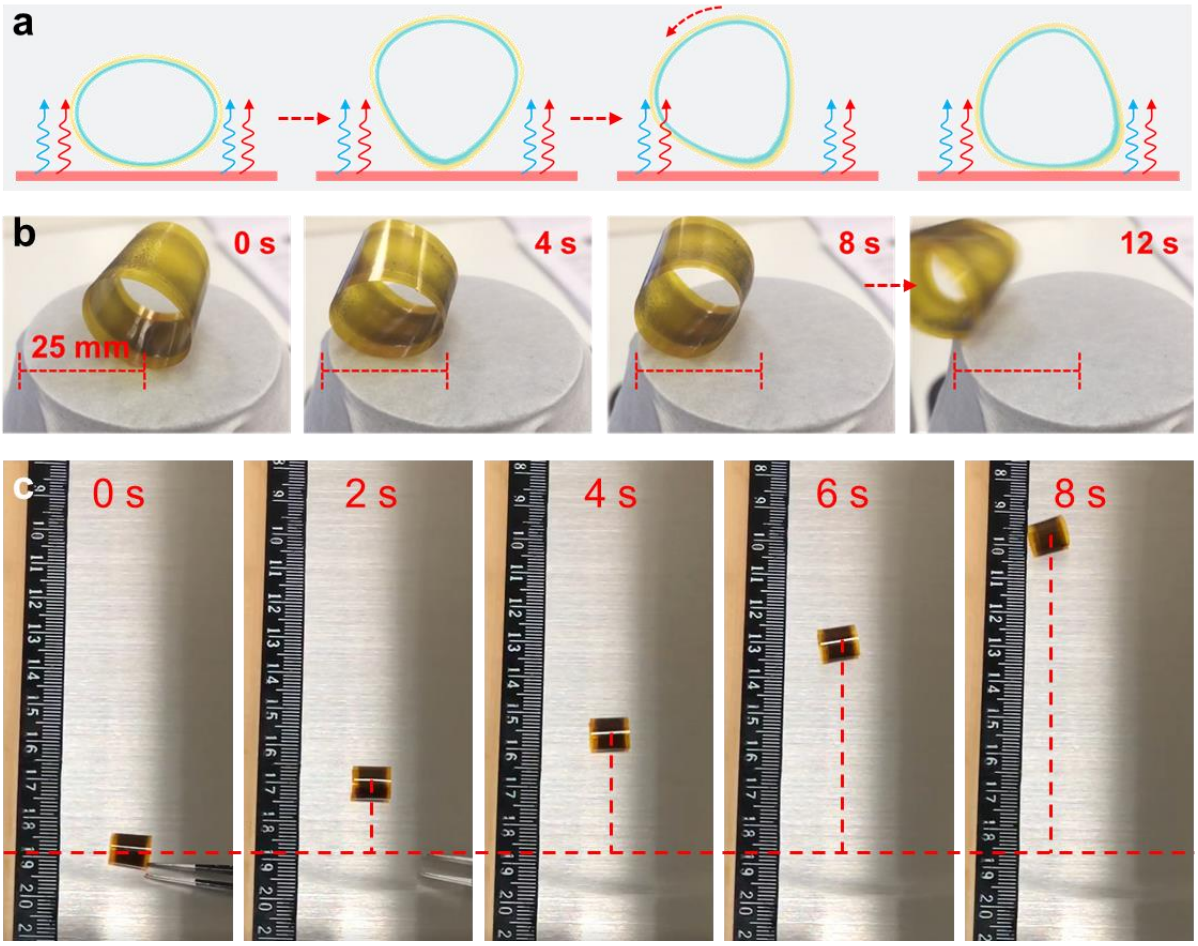

Fig. S14. (a) Schematics and (b) photographs illustrating the manipulation of the CNF-soft actuator as a walking robot. (c) Photographs showing the self-walking behavior of the wheel-like CNF-actuator on top of a 95 °C hot plate.

Estimation of the volumetric strain associated with the drying process of CNF

When a drop of CNF solution dries on a substrate, the evaporation process only starts to induce stress after the water content falls below a critical value at which the CNF experiences a phrase transit from the original solution state to a hydrogel state, and the CNFs begins to anchor at the interface at the substrate. The very first state of the evaporation of the CNF/water mixture in the solution form is stress-free. We postulate that the critical water content for the CNF solution to form CNF hydrogel equals the equilibrium moisture content (EMC) at very high relative humidity, for example, 80%~100%.

EMC is the maximum water content the CNF hydrogel sustains at a certain relative humidity (RH). Above EMC, no extra water molecule enters the CNF hydrogel system by bonding to CNF; instead, the extra water stays outside the hydrogel as free water content. Therefore, the presence of any extra water does not result in a change of the hydrogel volume, whereas the volumetric strain is related to the change of EMC in the CNF layer.

For a bulk wood material, according to Hailwood-Horrobin equation,[1] EMC can be evaluated as a function of temperature and RH. When the change in equilibrium moisture content ΔEMC is known, the volumetric strain can be estimated by the following equations,

$$V_0 = \frac{m_{\mathrm{CNF}}}{\rho_{\mathrm{CNF}}} + \frac{EMC_0 \times m_{\mathrm{CNF}}}{\rho_{\mathrm{water}}}$$

$$V_1 = \frac{m_{\mathrm{CNF}}}{\rho_{\mathrm{CNF}}} + \frac{EMC_1 \times m_{\mathrm{CNF}}}{\rho_{\mathrm{water}}}$$

$$\Delta\varepsilon_{\mathrm{v}} = \frac{\Delta V}{V_0} = \frac{V_0 - V_1}{V_0} = \frac{\Delta EMC}{\frac{\rho_{\mathrm{water}}}{\rho_{\mathrm{CNF}}} + EMC_1}$$

where V_0 is the original volume of CNF layer at a high moisture content EMC_0, V_1 is the volume at a lower moisture content EMC_1, $\Delta EMC = EMC_0 - EMC_1$ is the change in moisture content, m_{CNF}

is the mass of dry CNF, ρ_{water}=1.0 g cm^{-3} and ρ_{CNF} =1.2 g cm^{-3} are the densities of water and CNF respectively. At T=40°C, RH=80%, EMC=14.96%, and T=40°C, RH=45%, EMC=7.86%, the volumetric strain is 7.2%. When temperature increases to 80°C, if no moisture is added to the ambiance, the RH decreases to a very small value (RH = 5%), in this case, the volumetric strain estimated by Hailwood-Horrobin equation is about 14%. Therefore, from 40 to 80°C: $\Delta V/V_0$ = 7.2%~14%. In the calculation, we took the order of the magnitude of $\Delta\varepsilon_v$ to be ~10%.

Details of Finite Element Model

The contact between the bilayer is modeled as a surface-to-surface formation with "hard" contact behavior in the normal direction. In the tangential direction, the friction is modeled by prescribing a frictional coefficient of 0.09. In the very first step of the simulation, a small variation (less than 5%) of the prescribed volumetric strain in the longitudinal direction of the bilayer is prescribed, instead of using a uniform distribution, so that bilayer is able to close into a ring. (Otherwise due to the symmetry, the two ends of the bilayer will meet and interfere with each other) After the closure of the ring, the volumetric strain is corrected back to a uniform spatial distribution.

Reference

1. A. J. Hailwood, S. Horrobin, Trans. Faraday Soc. 1946, 42, 84. doi:10.1039/TF946420B084.